Breathing-Driven Metal-Insulator Transition in Correlated Kagome Systems

Qingzhuo Duan[1], Zixuan Jia[1], Zenghui Fan[1], Runyu Ma[1], Jingyao Meng[1], Bing Huang[1,2], and Tianxing Ma[1,3*]

[1]*School of Physics and Astronomy, Beijing Normal University, Beijing 100875, China*
[2]*Beijing Computational Science Research Center, Beijing 100084, China*
[3]*Key Laboratory of Multiscale Spin Physics (Ministry of Education), Beijing Normal University, Beijing 100875, China*

(Received 17 June 2025; accepted manuscript online 30 July 2025)

Inspired by the recent discovery of breathing kagome materials Nb_3Cl_8 and Nb_3TeCl_7, we have explored the influence of the breathing effect on the Hubbard model of the kagome lattice. Utilizing the determinant quantum Monte Carlo method, we first investigated the average sign problem in the breathing kagome lattice, which is influenced by both the breathing strength and the interaction strength. Secondly, we calculated the electronic kinetic energy, the direct current conductivity, and the electronic density of states at the Fermi level to determine the critical interaction strength for the metal–insulator transition. Our results indicate that the breathing effect, in conjunction with the interaction strength, drives the kagome system from a metal to an insulator. Finally, we evaluated the magnetic properties and constructed a phase diagram incorporating both transport and magnetic properties. The phase diagram reveals that as the interaction strength increases, the system transitions from a paramagnetic metal to a Mott insulator. Our research provides theoretical guidance for utilizing the breathing effect to control the band gaps, conductivity, and magnetic properties of kagome materials with electronic interactions.

DOI: 10.1088/0256-307X/42/9/090712 CSTR: 32039.14.0256-307X.42.9.090712

1. Introduction. The kagome lattice, distinguished by its unique corner-sharing triangular geometry, stands as a promising platform for investigating numerous correlated electron phenomena, encompassing the metal–insulator transition (MIT), magnetism, unconventional superconductivity, and quantum spin liquid states.[1–8] Over the past two decades, multiple families of kagome materials have garnered significant research attention owing to their fascinating MIT behaviors and magnetic properties.[9–11] This focus originates from their unique electronic structures and topological features, which render them critical platforms for deciphering the intricate interplay between electron correlations and phase transitions in condensed matter systems.[1,12]

Specifically, angle-resolved photoemission spectroscopy (ARPES) was employed to characterize RbV_3Sb_5, revealing that its charge density wave phase transition triggers the opening of partial energy gaps and the emergence of new Van Hove singularities.[1,2] Interestingly, the kagome material Nb_3Cl_8 was successfully exfoliated via mechanical methods,[13] where lattice distortion induced a breathing effect that opened the Dirac cone and introduced multiple band gaps. Subsequently, Nb_3TeCl_7 was synthesized using a solid-state approach,[14] with theoretical studies establishing that the on-site energy tunability of Nb sites modulates the bandwidth and topological structure of flat bands in this system. Additionally, the MIT can be induced by various modulation techniques. Adjusting the chemical potential in the $(Bi,Sb)_2Te_3$ channels results in a band insulator.[15] Furthermore, structural distortion under pressure triggers the MIT in $CrSiTe_3$.[16]

In terms of magnetic properties, most kagome materials exhibit antiferromagnetic (AFM) order, such as $ZnCu_3(OH)_6Cl_2$, FeGe, and YMn_6Sn_6.[12,17–19] Significantly, substituting rare earth atoms in zig-zag chains enables tuning of magnetic properties, for example, transitioning from the nonmagnetic state of $YbTi_3Bi_4$ to the ferromagnetic (FM) phase of $NdTi_3Bi_4$.[20,21] FM order has also been observed via ARPES in the d-electron kagome metal Fe_3Sn_2.[22] Given the above experimental studies, these advancements highlight the urgent need to elucidate the underlying physical mechanisms governing the MIT and magnetism in kagome systems, which has emerged as a pivotal research direction.[23,24]

A multitude of theoretical approaches have been employed to study the kagome systems. Within the framework of the tight-binding approximation,[25] the hexagonal rotational symmetry of the kagome lattice imparts opposite phases to the eigenfunctions at adjacent corners. This phase opposition leads to a cancellation of the phase during electron hopping between neighboring lattice sites, effectively confining electrons within the hexagonal units. The resulting electron localization gives rise to a pronounced electron correlation effect, and various numerical methodologies have been utilized to

*Corresponding author. Email: txma@bnu.edu.cn
© 2025 Chinese Physical Society and IOP Publishing Ltd. All rights, including for text and data mining, AI training, and similar technologies, are reserved.

investigate the kagome Hubbard model. These include the variational cluster approximation,[26,27] cellular dynamical mean-field theory,[28,29] variational Monte Carlo studies,[30,31] and determinant quantum Monte Carlo (DQMC) method.[32,33] Collectively, these studies concur that the system experiences a Mott transition at a critical interaction strength. However, the critical interaction strength U/t derived from these investigations ranges from 5 to 11, a discrepancy that may stem from the diverse strategies employed to refine the ground state approximations. Beyond kagome lattices, similar mechanisms of correlation-driven localization have been observed in other systems: strong correlations can drive the Lieb and graphene lattices from a metallic state to a Mott insulating state with an energy gap,[34,35] while disorder in lattice-site hopping processes leads to electron localization near the Fermi level, giving rise to an Anderson insulator.[36,37] These findings highlight the universality of electron correlation effects in modulating phase transitions across different lattice geometries.

Despite the diverse modulation techniques for the MIT discussed earlier, most kagome materials identified to date are gapless metals. This characteristic inherently prevents them from achieving an "off" state in devices,[12,38] imposing limitations on their applications in logic and optoelectronic systems. As a result, proposing effective methods to control the electronic transport properties of kagome materials has become an urgent research priority. In this context, an exciting advancement came in 2022 when Sun *et al.* successfully isolated a monolayer of Nb_3Cl_8 via mechanical exfoliation.[13] The three Nb atoms in this material spontaneously form a breathing kagome lattice, where electron cloud overlap is notably stronger within the unit cell than between unit cells. This structural feature breaks the sixfold rotational symmetry, leading to the opening of the Dirac cone and the introduction of multiple band gaps. Building on this, Zhang *et al.* synthesized Nb_3TeCl_7 by substituting Cl with Te in Nb_3Cl_8,[14] demonstrating that modulating the element at the Te site can tune the breathing effect strength and continuously adjust the band structure. These findings highlight a novel strategy for regulating the MIT and magnetic properties, underscoring the importance of investigating the combined roles of breathing and correlation effects in kagome lattices.

To address these research goals, we utilized the DQMC method to study the transport and magnetic properties of the Hubbard model on a breathing kagome lattice. This approach enables precise exploration of the relationship between quantum critical points and the breathing effect, while clarifying underlying physical mechanisms. The paper is structured as follows: Section 2 details the Hubbard Hamiltonian and key observables, with a focus on the DQMC method; Section 3 presents results showing that the breathing effect, in conjunction with interaction strength, drives the kagome system from a paramagnetic metal to a Mott insulator, as evidenced by calculations of kinetic energy, dc conductivity, and density of states, and constructs a phase diagram using correlation and breathing strengths; Section 4 summarizes the main conclusions that the breathing effect can be used to control the band gaps, conductivity, and magnetic properties of kagome materials with electronic interactions.

2. Model and Method. The Hamiltonian for a Hubbard model on an breathing kagome lattice is defined as

$$\begin{aligned} H = & -\sum_{\boldsymbol{r},\sigma}\{t_{\text{in}}[a^{\dagger}_{\boldsymbol{r},\sigma}b_{\boldsymbol{r},\sigma}+b^{\dagger}_{\boldsymbol{r},\sigma}c_{\boldsymbol{r},\sigma}+c^{\dagger}_{\boldsymbol{r},\sigma}a_{\boldsymbol{r},\sigma}] \\ & + t_{\text{ex}}[a^{\dagger}_{\boldsymbol{r},\sigma}b_{\boldsymbol{r}-\boldsymbol{x},\sigma}+b^{\dagger}_{\boldsymbol{r},\sigma}c_{\boldsymbol{r}+\boldsymbol{x}-\boldsymbol{y},\sigma}+c^{\dagger}_{\boldsymbol{r},\sigma}a_{\boldsymbol{r}+\boldsymbol{y},\sigma}]+\text{h.c.}\} \\ & -\mu\sum_{\boldsymbol{r},\sigma}n_{\boldsymbol{r},\sigma}+U\sum_{\boldsymbol{r}}n_{\boldsymbol{r},\uparrow}n_{\boldsymbol{r},\downarrow}. \end{aligned} \tag{1}$$

Here, $a_{\boldsymbol{r},\sigma}$ ($a^{\dagger}_{\boldsymbol{r},\sigma}$), $b_{\boldsymbol{r},\sigma}$ ($b^{\dagger}_{\boldsymbol{r},\sigma}$) and $c_{\boldsymbol{r},\sigma}$ ($c^{\dagger}_{\boldsymbol{r},\sigma}$) are the standard fermion annihilation (creation) operators at position $\boldsymbol{r}$ with spin σ, and $n_{\boldsymbol{r},\sigma}$ is the number operator. t_{in}, t_{ex}, μ, and U represent the hopping amplitude within the unit cell, the hopping amplitude between the unit cells, the chemical potential, and the on-site repulsive interaction, respectively. The sketch for the system that we simulated is shown in Fig. 1(a). To introduce the breathing effect in the lattice, we set $t_{\text{in}} = 1$ as the reference energy scale and vary t_{ex} from 0.5 to 1 in increments of 0.1.[13] At $t_{\text{ex}} = 1$, the system equivalents to a normal kagome lattice. As the value of t_{ex} decreases, the breathing strength is enhanced. Apart from the discussion on the finite size effect, we perform all calculations on a $3 \times L^2$ kagome lattice with a linear size of $L = 6$.

The DQMC method[39,40] was utilized to numerically investigate the MIT within the Hubbard model as defined by Eq. (1). As a nonperturbative approach, DQMC provides an exact numerical technique for examining the Hubbard model at finite temperatures. Initially, the partition function $Z = \text{Tr}\, e^{-\beta H}$ is considered as a path integral, which is discretized into $\Delta\tau$ slices within the imaginary time interval $(0, \beta)$. The inverse temperature is given by $\beta \equiv 1/(k_{\text{B}}T)$, with k_{B} denoting the Boltzmann constant. The kinetic energy term is quadratic, and the on-site interaction term can be decoupled into a quadratic form by employing a discrete Hubbard–Stratonovich (HS) field transformation. Subsequently, the partition function Z can be analytically transformed into the product of two fermion determinants by integrating the quadratic Hamiltonian term. These determinants correspond to the spin-up and spin-down states, respectively. To facilitate the sampling process, the Metropolis algorithm is employed with the time-slice interval $\Delta\tau$ set to 0.1, ensuring sufficiently small errors in the Trotter approximation. To assess the reliability of the computational results, we calculated the average fermion sign $\langle\text{sign}\rangle$ as a measure of the severity of the sign problem,

$$\langle\text{sign}\rangle = \frac{\sum_{\mathcal{X}} \det M_{\uparrow}(\mathcal{X})\det M_{\downarrow}(\mathcal{X})}{\sum_{\mathcal{X}} |\det M_{\uparrow}(\mathcal{X})\det M_{\downarrow}(\mathcal{X})|}, \tag{2}$$

Here, $\mathcal{X}$ represents the HS configurations, which consist of spatial sites and imaginary time slices. The matrix $M_{\sigma}(\mathcal{X})$ corresponds to the spin species. When $\langle\text{sign}\rangle = 1$, the system is free of the sign problem.

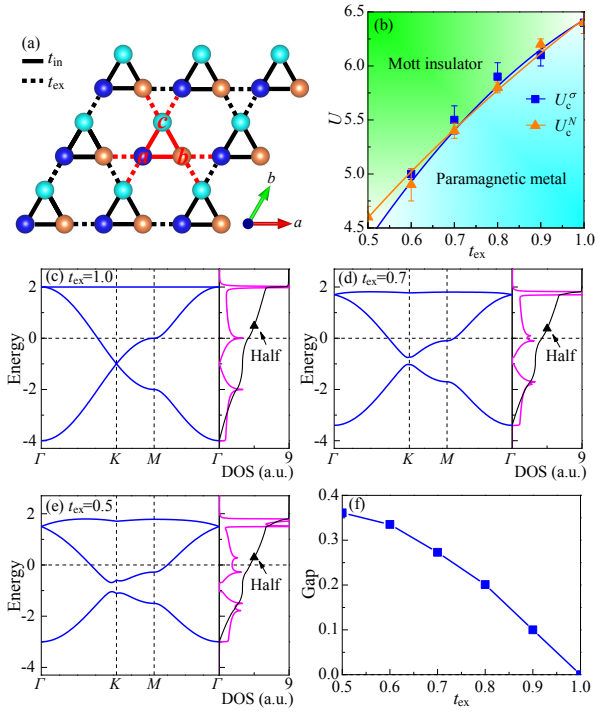

Fig. 1. (a) The lattice diagram of the breathing kagome system, with the unit cell and hopping processes highlighted in red. (b) The blue and orange curves correspond to the critical interaction strengths U_c^σ (U_c^N) for the MIT determined by the dc conductivity $\sigma_{\rm dc}(T)$ and by the density of states at the Fermi level $N(0)$, respectively. The green region above the U_c^σ curve represents the Mott insulating phase, while the blue region below the U_c^σ curve represents the paramagnetic metallic phase. (c)–(e) The band structures of the tight-binding model with $t_{\rm ex} = 1.0$, 0.7, and 0.5, respectively. (f) The gap at the Dirac cone as a function of $t_{\rm ex}$. Error bars are omitted when they are smaller than the symbol sizes.

To investigate the MIT in the breathing kagome lattice, we computed the temperature-dependent dc conductivity. This quantity can be derived from the current–current correlation function, which is momentum $\boldsymbol{q}$-dependent and imaginary time τ-dependent, denoted as $\Lambda_{xx}(\boldsymbol{q},\tau)$,[32,41,42]

$$\sigma_{\rm dc}(T) = \frac{\beta^2}{\pi}\Lambda_{xx}\Big(\boldsymbol{q}=0,\,\tau=\frac{\beta}{2}\Big). \tag{3}$$

Here, $\beta = 1/T$, $\Lambda_{xx}(\boldsymbol{q},\tau) = \langle j_x(\boldsymbol{q},\tau)j_x(-\boldsymbol{q},0)\rangle$, where $j_x(\boldsymbol{q},\tau)$ is the Fourier transform of the unequal-time current-0current correlation functions,

$$j_x(\boldsymbol{q},\tau) = \mathrm{e}^{H\tau}\Big[\mathrm{i}\sum_\sigma t_{\boldsymbol{q}+\boldsymbol{x},\boldsymbol{q}}(c^\dagger_{\boldsymbol{q}+\boldsymbol{x},\sigma}c_{\boldsymbol{q},\sigma} - c^\dagger_{\boldsymbol{q},\sigma}c_{\boldsymbol{q}+\boldsymbol{x},\sigma})\Big]\mathrm{e}^{-H\tau}. \tag{4}$$

The validity of Eq. (3) has been widely established in numerous studies of the Hubbard model.[43–48]

We also calculated the kinetic energy per site, which can be readily obtained by averaging the hopping terms,

$$\begin{aligned}\langle K\rangle = &-\frac{1}{N}\sum_{\boldsymbol{r},\sigma}\{t_{\rm in}[a^\dagger_{\boldsymbol{r},\sigma}b_{\boldsymbol{r},\sigma} + b^\dagger_{\boldsymbol{r},\sigma}c_{\boldsymbol{r},\sigma} + c^\dagger_{\boldsymbol{r},\sigma}a_{\boldsymbol{r},\sigma}]\\ &+ t_{\rm ex}[a^\dagger_{\boldsymbol{r},\sigma}b_{\boldsymbol{r}-\boldsymbol{x},\sigma} + b^\dagger_{\boldsymbol{r},\sigma}c_{\boldsymbol{r}+\boldsymbol{x}-\boldsymbol{y},\sigma} + c^\dagger_{\boldsymbol{r},\sigma}a_{\boldsymbol{r}+\boldsymbol{y},\sigma}]\\ &+ \text{h.c.}\}.\end{aligned} \tag{5}$$

To avoid complex numerical analytical continuation methods, the investigation of the density of states is focused on the Fermi level,

$$N(0) \approx \beta \times G(\boldsymbol{r}=0,\,\tau=\beta/2). \tag{6}$$

Here, $G(\boldsymbol{r},\tau)$ is the imaginary-time dependent Green's function. To investigate the magnetic properties of the breathing kagome lattice, we calculated the real-space spin–spin correlation functions,[34,49]

$$c^{\alpha\beta}(\boldsymbol{r}) = \frac{1}{3}\langle \boldsymbol{S}^\alpha_{\boldsymbol{r}_0}\cdot\boldsymbol{S}^\beta_{\boldsymbol{r}_0+\boldsymbol{r}}\rangle, \tag{7}$$

where $\boldsymbol{r}_0$ denotes the position of any lattice site, while $\boldsymbol{r}$ represents the distance between two sites. The indices α and β label the sites a, b or c. After performing a Fourier transform on $c^{\alpha\beta}(\boldsymbol{r})$, we obtain the magnetic structure factor

$$S(\boldsymbol{q}) = \frac{1}{N_{\rm s}}\sum_{\alpha,\beta}\sum_{\boldsymbol{r}} c^{\alpha\beta}(\boldsymbol{r})\mathrm{e}^{\mathrm{i}\boldsymbol{q}\cdot\boldsymbol{r}}, \tag{8}$$

in which $N_{\rm s} = 3L^2$ represents the total number of sites and L denotes the linear size of the lattice. Furthermore, the uniform magnetic susceptibility is directly related to the magnetic structure factor,

$$\chi \equiv \beta S(\boldsymbol{q}=0). \tag{9}$$

3. Result and Discussion. DQMC is an unbiased method, but it is plagued by the notorious minus-sign problem, which results in noisy averages.[50,51] This issue is absent in half-filled systems that possess particle–hole symmetry (PHS), such as bipartite lattices like square and honeycomb lattices. However, the kagome lattice is non-bipartite and lacks PHS for any filling, leading to a severe sign problem that depends on the system size, temperature scale, and interaction strength. In present work, we investigated this system at half-filling with the average electron density $n = 1$ per site, which represents a regime of significant interest. Figure 2 shows how the chemical potential leading to a half-filled case at different U changes with temperature. To determine the proper Monte Carlo parameters rely on the sign problem, we firstly present the average sign $\langle\text{sign}\rangle$ as a function of temperature T on the breathing kagome lattice with 3×6^2 sites for various U values in Figs. 3(a)–3(c). For the same T, $\langle\text{sign}\rangle$ is significantly suppressed as $t_{\rm ex}$ decreases, indicating that a larger breathing effect greatly exacerbates the sign problem. Figure 3(d) shows the differences in $\langle\text{sign}\rangle$ between $t_{\rm ex} = 1.0$ and $t_{\rm ex} = 0.5$ for three U values, defined as $\Delta\langle\text{sign}\rangle = \langle\text{sign}\rangle_{t_{\rm ex}=1.0} - \langle\text{sign}\rangle_{t_{\rm ex}=0.5}$. When $U = 4$, $\Delta\langle\text{sign}\rangle$ continuously increases as T decreases. However, when U is increased to values above 5, $\Delta\langle\text{sign}\rangle$ first increases to a peak and then begins to decrease. At high temperatures, the average sign $\langle\text{sign}\rangle$ remains close to 1, ensuring reliable numerical data. As temperature decreases, $\langle\text{sign}\rangle$ diminishes, reflecting the worsening sign problem. When $\langle\text{sign}\rangle > 0.5$, the sign problem remains mild and permits accurate results. For severe cases where $\langle\text{sign}\rangle < 0.5$,

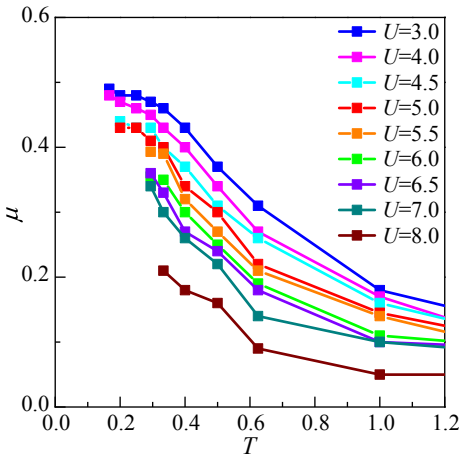

Fig. 2. The chemical potential that leads to the half filling of the system as a function of the temperature for different values of interaction strengths.

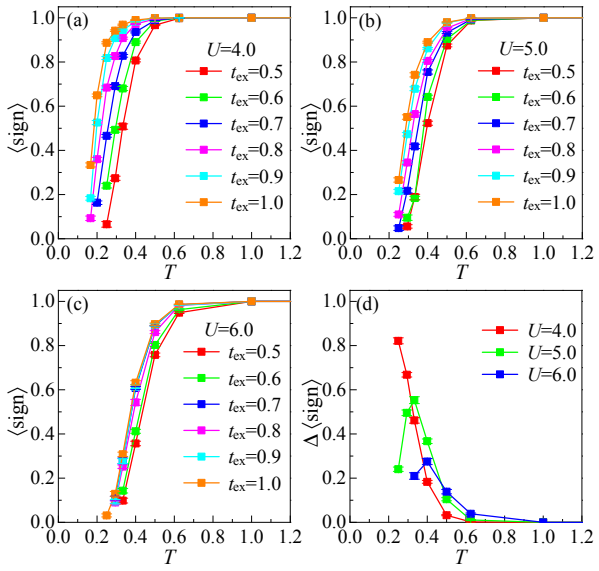

Fig. 3. (a)–(c) The average sign $\langle \text{sign} \rangle$ as a function of temperature T for $U = 4.0$, 5.0, and 6.0, respectively. (d) The differences in the average sign $\langle \text{sign} \rangle$ between $t_{\text{ex}} = 1.0$ and $t_{\text{ex}} = 0.5$ for various U values, denoted as $\Delta\langle \text{sign} \rangle$. Error bars are omitted when they are smaller than the symbol sizes.

extended Monte Carlo runs compensate for increased fluctuations within the DQMC framework. We therefore implement substantially longer simulations when $\langle \text{sign} \rangle$ falls below 0.5.[39,52]

For an infinite lattice with only nearest-neighbor hopping, the band structures of the kagome lattice with the breathing effect are shown in Figs. 1(c)–1(e). When $t_{\text{ex}} = 1.0$ [see Fig. 1(c)], the band structure contains one flat band, one Dirac cone, and two van Hove singularities located at $E = 2$, -1, 0, and -2, respectively. When the system is half-filled, the Fermi level (marked by the black triangle) is located at $E = 0.48$, and the corresponding density of states is 1.23. As t_{ex} is reduced to 0.7 and then to 0.5 [see Figs. 1(d) and 1(e)], the density of states at the Fermi level remains non-zero. Thus, the system remains metallic as t_{ex} decreases from 1 to 0.5. Meanwhile, the breathing effect opens a gap at the Dirac cone, and the gap widens as t_{ex} decreases [see Fig. 1(f)]. The gap, induced by the breathing effect, will diminish the metallic character of the system.

To investigate the transport properties of the kagome lattice when both the breathing effect and correlated interactions are introduced simultaneously, we first examine the kinetic energy. Figure 4(a) displays the kinetic energy per site $\langle K \rangle$ for the normal kagome lattice for various U values. The $\langle K \rangle$ increases with increasing T and U, suggesting that fermions tend to localize and the system gradually approaches an insulating state. However, up to $U = 8$, the system still does not exhibit $\frac{\partial K(T)}{\partial T} < 0$. Thus, the behavior of the kinetic energy only indicates a tendency for the kagome lattice to transition towards an insulator, consistent with previous investigations.[32] Figures 4(b)–4(d) show the kinetic energy including the breathing effect for various U values. It is evident that $\langle K \rangle$ increases monotonically with decreasing t_{ex}, but $\frac{\partial K(T)}{\partial T} < 0$ still does not appear. Therefore, $\langle K \rangle$ does not reflect the MIT of this system.

Given the above situation, other quantities should be investigated to identify the phase transition. Therefore, we proceed to examine the dc conductivity σ_{dc} as a function of temperature T, computed across several representative sets of U and t_{ex} as shown in Fig. 5. As illustrated in Fig. 5(a), when $U < 6.5$, $\frac{\partial \sigma_{\text{dc}}(T)}{\partial T} < 0$ as T increases, and $\sigma_{\text{dc}}(T)$ diverges as T approaches 0, indicating that the system exhibits metallic behavior. However, when $U \geq 6.5$, $\frac{\partial \sigma_{\text{dc}}(T)}{\partial T} > 0$ at low T, which is a signature of fermion localization. This indicates that the system transitions from a metal to an insulator. In this case, we determine the critical interaction strength for the MIT defined by the conductivity as $U_{\text{c}}^{\sigma} = 6.40 \pm 0.10$ for $t_{\text{ex}} = 1.0$.

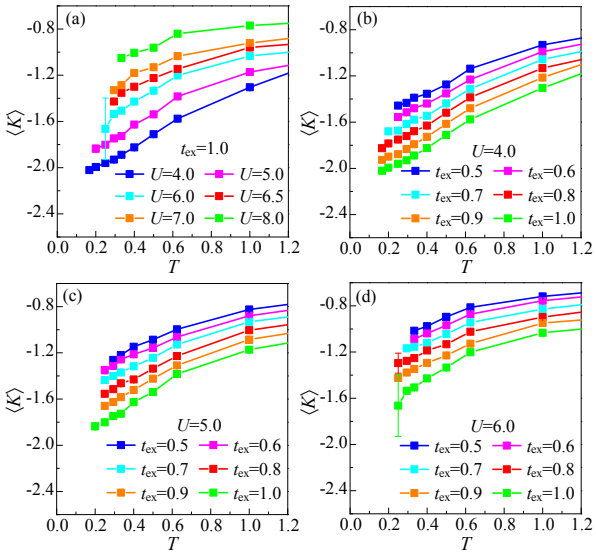

Fig. 4. (a) The kinetic energy per site $\langle K \rangle$ for the normal kagome lattice ($t_{\text{ex}} = 1.0$) as a function of temperature T for various U values. (b)–(d) The kinetic energy per site $\langle K \rangle$ for the breathing kagome lattice with $U = 4.0$, 5.0, and 6.0, respectively. Error bars are omitted when they are smaller than the symbol sizes.

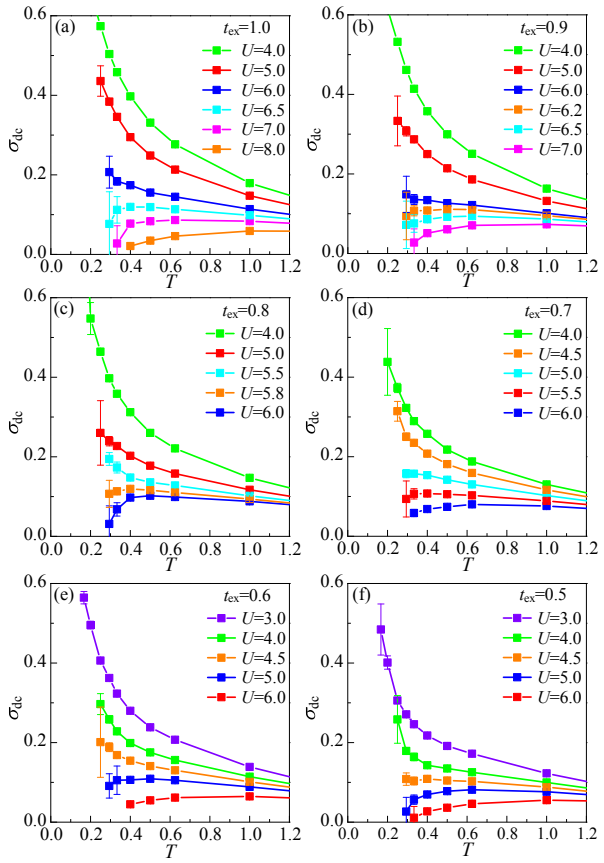

Fig. 5. The dc conductivity $\sigma_{\rm dc}$ as a function of temperature T for (a) $t_{\rm ex} = 1.0$, (b) $t_{\rm ex} = 0.9$, (c) $t_{\rm ex} = 0.8$, (d) $t_{\rm ex} = 0.7$, (e) $t_{\rm ex} = 0.6$, and (f) $t_{\rm ex} = 0.5$, respectively. Error bars are omitted when they are smaller than the symbol sizes.

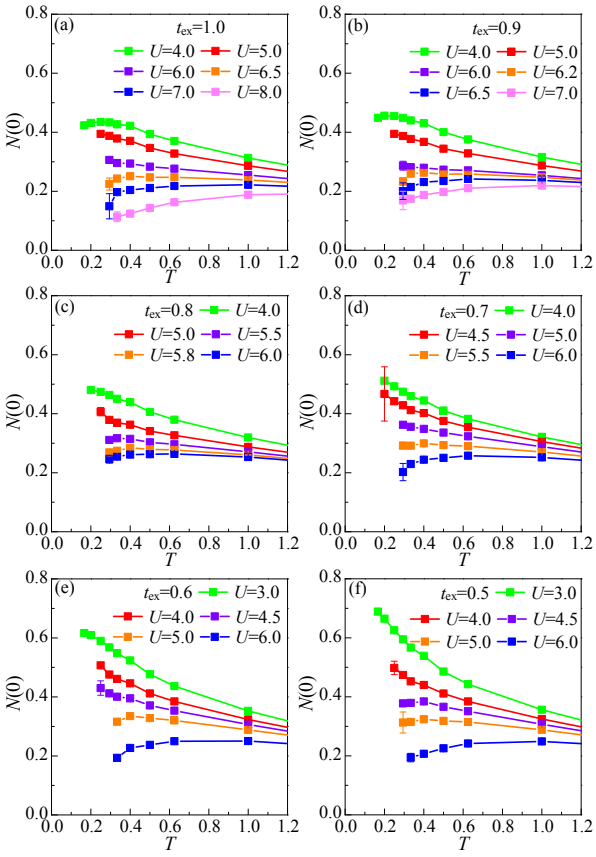

Fig. 6. The density of states at the Fermi level, $N(0)$, as a function of temperature T for (a) $t_{\rm ex} = 1.0$, (b) $t_{\rm ex} = 0.9$, (c) $t_{\rm ex} = 0.8$, (d) $t_{\rm ex} = 0.7$, (e) $t_{\rm ex} = 0.6$, and (f) $t_{\rm ex} = 0.5$, respectively. Error bars are omitted when they are smaller than the symbol sizes.

These results are consistent with the preceding study about the normal kagome lattice.[32] Figures 5(b)–5(f) show the $\sigma_{\rm dc}(T)$ for various values of $t_{\rm ex}$. Using the same criterion to determine $U_{\rm c}^{\sigma}$, we find that $U_{\rm c}^{\sigma}$ decreases monotonically with decreasing $t_{\rm ex}$. The study of the band structure suggests that the breathing effect diminishes the metallic character of the system, which may help to understand why $U_{\rm c}^{\sigma}$ decreases with the decrease of $t_{\rm ex}$. Based on these results, we determine the boundary between the metallic and insulating phases, denoted by $U_{\rm c}^{\sigma}$, as shown in Fig. 1(b). These findings indicate that the breathing effect reduces the critical interaction strength required for the MIT in the correlated kagome system.

We have analyzed the role of different terms in Eq. (1) in driving the MIT by examining $\sigma_{\rm dc}(T)$. This analysis is further corroborated by the behavior of the density of states at the Fermi level, $N(0)$, as $t_{\rm ex}$ is varied. Figure 6(a) presents $N(0)$ for $t_{\rm ex} = 1.0$. For $U < 6.5$, the $\frac{\partial N(0,T)}{\partial T} < 0$ and $N(0,T)$ diverges in the limit as T tends to 0. This behavior is characteristic of a metallic phase. In contrast, when $U \geq 6.5$, the derivative $\frac{\partial N(0,T)}{\partial T}$ becomes positive at low temperatures, indicating a transition to an insulating phase. Thus, the critical interaction strength for the MIT, as determined by $N(0)$, is $U_{\rm c}^{N} = 6.40 \pm 0.10$ for $t_{\rm ex} = 1.0$. Figures 6(b)–6(f) show the $N(0)$ for various values of $t_{\rm ex}$. Using the same methodology, we have analyzed the $U_{\rm c}^{N}$ for various values of $t_{\rm ex}$, and plotted a boundary separating the metallic and insulating phases, as shown in Fig. 1(b). This boundary is in excellent agreement with the MIT boundary obtained from the $\sigma_{\rm dc}(T)$ analysis.

To investigate the magnetic properties of the breathing kagome lattice, we examine the behavior of the spin–spin correlation function $c^{bc}(r = 1)$ between the nearest b and c sites as the $t_{\rm ex}$ decreased for various U [see Figs. 7(a)–7(d)]. For all values of U and temperature T, the correlation function $c^{bc}(r = 1)$ monotonically decreases from negative values as $t_{\rm ex}$ decreased. When $t_{\rm ex}$ and U are held constant, the magnitude of $c^{bc}(r = 1)$ increases as the temperature decreases. This indicates the emergence of magnetic order at low temperatures. Similarly, for a fixed $t_{\rm ex}$ and T, the magnitude of $c^{bc}(r = 1)$ increases with increasing U. This trend reflects that stronger repulsive interactions favor electron localization, thereby enhancing magnetic ordering. The spin–spin correlation function $c^{bb}(r = 2)$ for the next-nearest neighbors between b sites is depicted in Figs. 7(e)–7(h). We observe that $c^{bb}(r = 2)$ is at least one order of magnitude smaller than $c^{bc}(r = 1)$. For $U = 3.0$ and $U = 4.0$, as shown in Figs. 7(e) and 7(f), the decrease of $t_{\rm ex}$ causes the longer-range correlations to shift slightly towards positive values. When U exceeds 5.0, $c^{bb}(r = 2)$ gradually evolves into a weak FM correlation.

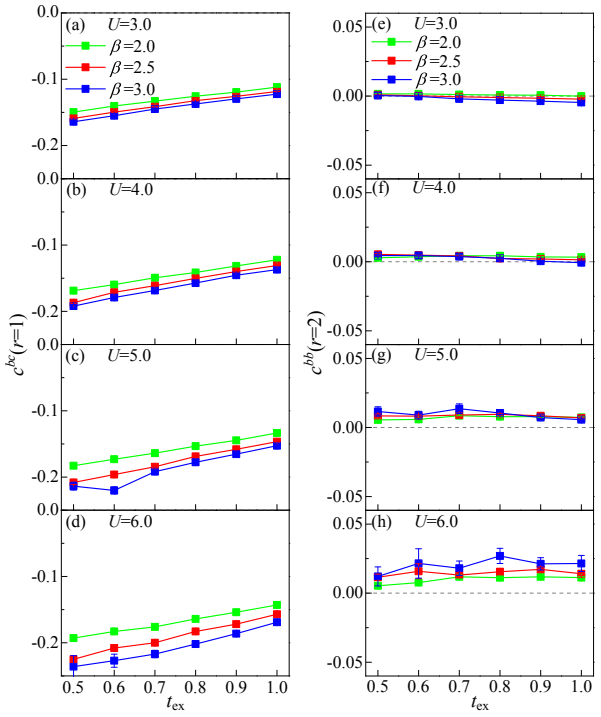

Fig. 7. The spin–spin correlations on the nearest b and c sites, $c^{bc}(r=1)$, for (a) $U=3.0$, (b) $U=4.0$, (c) $U=5.0$, and (d) $U=6.0$, respectively. The spin–spin correlations on the next-nearest b sites, $c^{bb}(r=2)$, for (e) $U=3.0$, (f) $U=4.0$, (g) $U=5.0$, and (h) $U=6.0$, respectively. Error bars are omitted when they are smaller than the symbol sizes.

These observations lead us to conclude that the kagome lattice exhibits strong short-range AFM correlations, which are enhanced as t_{ex} decreases and U increases. Meanwhile, the system has an extremely weak long-range FM correlation at low t_{ex} and high U. Overall, the AFM state consistently dominates the system, regardless of the values of t_{ex} and U. This conclusion is consistent with most of the experimentally discovered kagome materials, including $ZnCu_3(OH)_6Cl_2$, FeGe, and YMn_6Sn_6.[12,17–19]

The above conclusions are further substantiated by the temperature dependence of the uniform susceptibility χ for various U. As shown in Fig. 8, the χ increases as the t_{ex} decreases and U increases, but they do not reach a divergent level. This indicates that the system consistently displays AFM correlations for any values of t_{ex} and U. Combining the analyses of the MIT and magnetic properties, we present a phase diagram in Fig. 1(b). For U values above the boundary (U_c^{σ}), the conductivity of the system is suppressed, and AFM correlations are strong. We therefore designate this region as the Mott insulating phase. Conversely, when U drops below this boundary, the system exhibits metallic behavior while maintaining the AFM state. This region is thus identified as the paramagnetic metallic phase.

To ensure overall computational convergence, we examined the finite size effect on the σ_{dc} and $c^{bc}(r=1)$. In Figs. 9(a) and 9(b), we showed the σ_{dc} as a function of T for different sizes with $t_{ex}=1.0$ and 0.8.

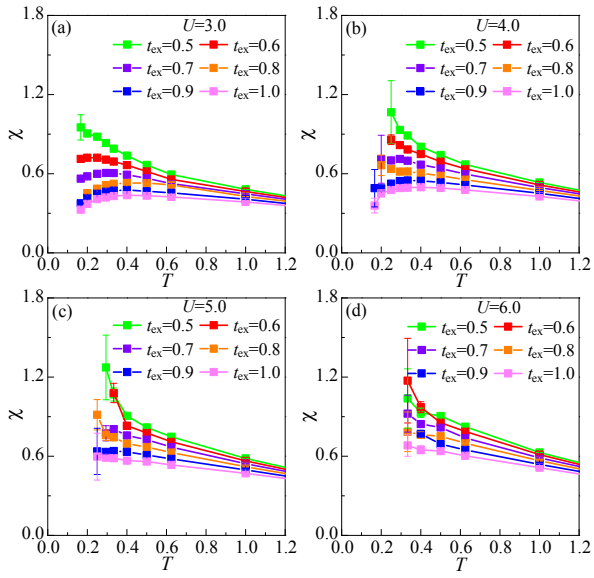

Fig. 8. The temperature dependence of the uniform susceptibility χ for (a) $U=3.0$, (b) $U=4.0$, (c) $U=5.0$, and (d) $U=6.0$, respectively, as t_{ex} decreases from 1.0 to 0.5. Error bars are omitted when they are smaller than the symbol sizes.

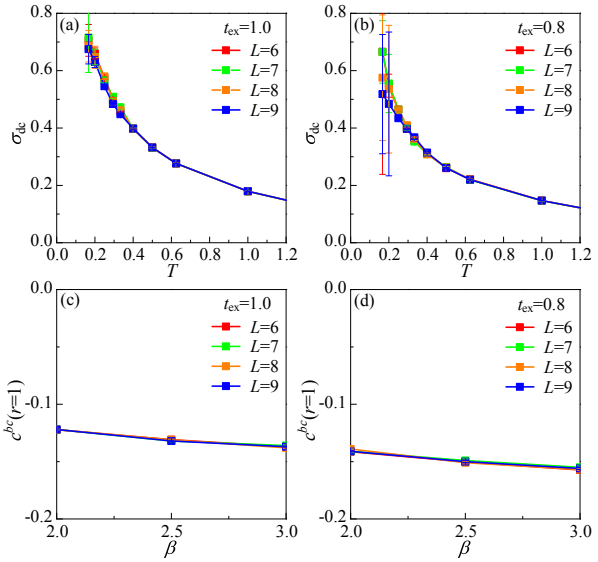

Fig. 9. (a) and (b) The dc conductivity σ_{dc} as a function of T for $t_{ex}=1.0$ and $t_{ex}=0.8$, with lattice size increases from 6 to 9. (c) and (d) The spin–spin correlations on the nearest b and c sites $c^{bc}(r=1)$ as a function of β for $t_{ex}=1.0$ and $t_{ex}=0.8$, with lattice size increases from 6 to 9.

The results indicate that the lattice size has little effect on σ_{dc}. On the other hand, figures 9(c) and 9(d) show the $c^{bc}(r=1)$ as a function of β for different sizes with $t_{ex}=1.0$ and 0.8. It can be seen that the $c^{bc}(r=1)$ of all sizes almost completely overlap. These results demonstrate that our calculations are well converged and reliable.[53]

4. Conclusion. Using DQMC simulations, we investigated the MIT and magnetic properties of the Hubbard model on a kagome lattice with introduced breathing effect. The breathing effect is realized by modulating the hopping amplitude between lattice sites. The critical interaction strength for the MIT is determined jointly by

the calculated electronic kinetic energy, dc conductivity, and the density of electronic states at the Fermi level. Moreover, our analysis of the magnetic properties indicates that the kagome lattice consistently exhibits an AFM state, which is enhanced by the breathing effect and the correlation interaction. By integrating the magnetic and transport responses, we constructed a phase diagram parameterized by U and $t_{\rm ex}$. The region above the boundary U_c^σ is identified as a Mott insulating phase, while the region below the boundary is characterized as a paramagnetic metallic phase. Recent realization of the Mott insulating phase in organic Kagome structures,[54] and the synthesis of breathing Kagome materials Nb_3Cl_8 and Nb_3TeCl_7,[13,14] have the potential to validate our theoretical framework. In addition, first-principles calculations and random phase approximation analyses have been used to predict that the sublattice-momentum coupling will enhance AFM fluctuations,[55] which draws conclusions similar to our theoretical studies. Our study provides valuable insights into the mechanisms underlying the MIT and magnetic properties in kagome systems. Additionally, the breathing effect could offer a novel strategy for tuning conductivity and magnetism in strongly correlated materials.

Acknowledgments. This work was supported by the National Science Foundation of China (Grant No. 12474218) and Beijing Natural Science Foundation (Grant Nos. 1242022 and 1252022). The numerical simulations in this work were performed at the HSCC of Beijing Normal University.

References

[1] Liu Z H, Zhao N N, Yin Q W *et al.* 2021 *Phys. Rev. X* **11** 041010
[2] Cho S, Ma H Y, Xia W *et al.* 2021 *Phys. Rev. Lett.* **127** 236401
[3] Yi S H, Liao Z Y, Wang Q *et al.* 2025 *Phys. Rev. Lett.* **134** 086902
[4] Chen H, Yang H T, Hu B *et al.* 2021 *Nature* **599** 222
[5] Balents L 2010 *Nature* **464** 199
[6] Han T H, Helton J S, Chu S Y, Nocera D G, Rodriguez-Rivera J A, Broholm C, and Lee Y S 2012 *Nature* **492** 406
[7] Fu M X, Imai T, Han T H, and Lee Y S 2015 *Science* **350** 655
[8] Chen K Y, Wang N N, Yin Q W, Gu Y H, Jiang K, Tu Z J, Gong C S, Uwatoko Y, Sun J P, Lei H C, Hu J P, and Cheng J G 2021 *Phys. Rev. Lett.* **126** 247001
[9] Hu Y, Le C C, Zhang Y H *et al.* 2023 *Nat. Phys.* **19** 1827
[10] Le T, Pan Z M, Xu Z K *et al.* 2024 *Nature* **630** 64
[11] Acharya G, Neupane B, Hsu C H *et al.* 2024 *Adv. Mater.* **36** 2410655
[12] Teng X K, Chen L B, Ye F *et al.* 2022 *Nature* **609** 490
[13] Sun Z Y, Zhou H, Wang C X *et al.* 2022 *Nano Lett.* **22** 4596
[14] Zhang H R, Shi Z J, Jiang Z C *et al.* 2023 *Adv. Mater.* **35** 2301790
[15] Lee J S, Richardella A, Reifsnyder Hickey D, Mkhoyan K A, and Samarth N 2015 *Phys. Rev. B* **92** 155312
[16] Musfeldt J L, Mandrus D G, and Liu Z 2023 *npj 2D Mater. Appl.* **7** 28
[17] Helton J S, Matan K, Shores M P *et al.* 2007 *Phys. Rev. Lett.* **98** 107204
[18] Ghimire N J, Dally R L, Poudel L *et al.* 2020 *Sci. Adv.* **6** eabe2680
[19] Wang Q, Neubauer K J, Duan C *et al.* 2021 *Phys. Rev. B* **103** 014416
[20] Chen L, Zhou Y, Zhang H *et al.* 2024 *Commun. Mater.* **5** 73
[21] Yin J X, Lian B, and Hasan M Z 2022 *Nature* **612** 647
[22] Ye L D, Kang M G, Liu J W *et al.* 2018 *Nature* **555** 638
[23] Wu X X, Schwemmer T, Müller T *et al.* 2021 *Phys. Rev. Lett.* **127** 177001
[24] Tan H X, Liu Y Z, Wang Z Q, and Yan B H 2021 *Phys. Rev. Lett.* **127** 046401
[25] Wang Y J, Wu H, McCandless G T, Chan J Y, and Ali M N 2023 *Nature Rev. Phys.* **5** 635
[26] Higa R and Asano K 2016 *Phys. Rev. B* **93** 245123
[27] Seki K, Shirakawa T, and Yunoki S 2018 *Phys. Rev. B* **98** 205114
[28] Ohashi T, Kawakami N, and Tsunetsugu H 2006 *Phys. Rev. Lett.* **97** 066401
[29] Klett M, Wentzell N, Schäfer T, Simkovic F, Parcollet O, Andergassen S, and Hansmann P 2020 *Phys. Rev. Res.* **2** 033476
[30] Kuratani S, Koga A, and Kawakami N 2007 *J. Phys. Cond. Matter* **19** 145252
[31] He L W, Yu S L, and Li J X 2024 *Phys. Rev. Lett.* **133** 096501
[32] Medeiros-Silva A R, Costa N C, and Paiva T 2023 *Phys. Rev. B* **107** 035134
[33] Ding S H, Li S Z, and Wang Y 2025 *Commun. Phys.* **8** 48
[34] Lima L O, Medeiros-Silva A R, dos Santos R R, Paiva T, and Costa N C 2023 *Phys. Rev. B* **108** 235163
[35] Ma T X, Zhang L F, Chang C C, Hung H H, and Scalettar R T 2018 *Phys. Rev. Lett.* **120** 116601
[36] Li J, Chu R L, Jain J K, and Shen S Q 2009 *Phys. Rev. Lett.* **102** 136806
[37] Meng J Y, Mondaini R, Ma T X, and Lin H Q 2021 *Phys. Rev. B* **104** 045138
[38] Kang M G, Fang S A, Kim J K *et al.* 2022 *Nat. Phys.* **18** 301
[39] Blankenbecler R, Scalapino D J, and Sugar R L 1981 *Phys. Rev. D* **24** 2278
[40] White S R, Scalapino D J, Sugar R L, Loh E Y, Gubernatis J E, and Scalettar R T 1989 *Phys. Rev. B* **40** 506
[41] Denteneer P J H, Scalettar R T, and Trivedi N 1999 *Phys. Rev. Lett.* **83** 4610
[42] Trivedi N, Scalettar R T, and Randeria M 1996 *Phys. Rev. B* **54** R3756
[43] Tian L Y, Li Y Q, Liang Y, and Ma T X 2022 *Phys. Rev. B* **105** 045132
[44] Guo K Y, Liang Y, and Ma T X 2024 *Phys. Rev. B* **109** 045107
[45] Wang J Y, Zhang L F, Ma R Y, Chen Q N, Liang Y, and Ma T X 2020 *Phys. Rev. B* **101** 245161
[46] Trivedi N and Randeria M 1995 *Phys. Rev. Lett.* **75** 312
[47] Iglovikov V I, Hébert F, Grémaud B, Batrouni G G, and Scalettar R T 2014 *Phys. Rev. B* **90** 094506
[48] Pan Y, Ma R Y, and Ma T X 2023 *Phys. Rev. B* **107** 245126
[49] Liang S D, Wang Z D, Wang Q, and Shen S Q 1999 *Phys. Rev. B* **59** 3321
[50] Loh E Y, Gubernatis J E, Scalettar R T, White S R, Scalapino D J, and Sugar R L 1990 *Phys. Rev. B* **41** 9301
[51] Troyer M and Wiese U J 2005 *Phys. Rev. Lett.* **94** 170201
[52] Yang G, Xu S L, Zhang W, Ma T X, and Wu C J 2016 *Phys. Rev. B* **94** 075106
[53] Tian L Y, Meng J Y, and Ma T X 2022 *Phys. Rev. B* **106** 205144
[54] Lowe B, Field B, Hellerstedt J, Ceddia J, Nourse H L, Powell B J, Medhekar N V, and Schiffrin A 2024 *Nat. Commun.* **15** 3559
[55] Wu S Q, Xu C C, Wang X Q, Lin H Q, Cao C, and Cao G H 2025 *Nat. Commun.* **16** 1375